



Cite this: *Chem. Sci.*, 2025, **16**, 14468

All publication charges for this article have been paid for by the Royal Society of Chemistry

Received 21st April 2025  
Accepted 22nd June 2025

DOI: 10.1039/d5sc02886h  
[rsc.li/chemical-science](http://rsc.li/chemical-science)

## Introduction

Hydrogen energy offers a promising solution to the global environmental and energy crises,<sup>1,2</sup> with hydrogen fuel cells emerging as a leading technology for efficient energy conversion.<sup>3–7</sup> Compared with proton exchange membrane fuel cells, alkaline exchange membrane fuel cells (AEMFCs) have garnered much attention due to the development of anion exchange membranes and the facile use of Pt group metal (PGM)-free catalysts for the cathode ORR.<sup>6,8–10</sup> Nevertheless, the hydrogen oxidation reaction (HOR) at the anode on a PGM catalyst is approximately two to three orders of magnitude slower in alkaline media than in acid.<sup>11–13</sup> Recent efforts to develop alkaline HOR electrocatalysts have largely focused on

PGMs and their alloys. However, the high cost and limited HOR kinetic activity of Pt-based HOR catalysts severely hinder their practical application in AEMFCs. Consequently, Ru-based catalysts have emerged as a promising alternative, possessing a comparable affinity for H<sub>2</sub> to that of Pt while being more cost-effective (about 50% of Pt price),<sup>14,15</sup> and showing higher oxygen tolerance compared to Ni-based alternatives.<sup>16,17</sup>

To boost the HOR activity of Ru-based catalysts, extensive structural engineering strategies have been explored, including interface engineering,<sup>18–22</sup> heteroatom incorporation,<sup>23–26</sup> strain engineering and single atom construction.<sup>27–29</sup> Among these, strain engineering can modulate the catalytic performance through tensile or compressive strains, induced by lattice mismatch in designed core shells, alloyed nanostructures or twin structures like icosahedra.<sup>14,30</sup> Studies have proved that strain can alter the d-band center and modulate the surface binding to the reaction intermediates.<sup>14,31</sup> For instance, PdCu/Ir core-shell catalysts, which eliminate electronic effects and retain 3.6% compressive strain, exhibit excellent OER activity.<sup>32</sup> However, for strained catalysts in the HOR, the interplay between the strain effect and electronic effect remains difficult to disentangle.<sup>24,27,33–36</sup> In a notable case, Shao and co-workers reported that HOR activity of Ru-modified Pt correlates with Ru coverage, where both strain and electronic effects strengthen the binding of \*H and OH\*.<sup>37</sup> The challenge in isolating the strain effect from these other factors has hindered a clear understanding of its independent contribution to the HOR. To date, a comprehensive analysis of the strain effect in the HOR is

<sup>a</sup>College of Materials Science and Engineering, Hunan University, Changsha, Hunan 410082, P. R. China

<sup>b</sup>Key Laboratory of Mesoscopic Chemistry of MOE and Jiangsu Provincial Lab for Nanotechnology, School of Chemistry and Chemical Engineering, Nanjing University, Nanjing, Jiangsu 210023, P. R. China. E-mail: huanghw@nju.edu.cn

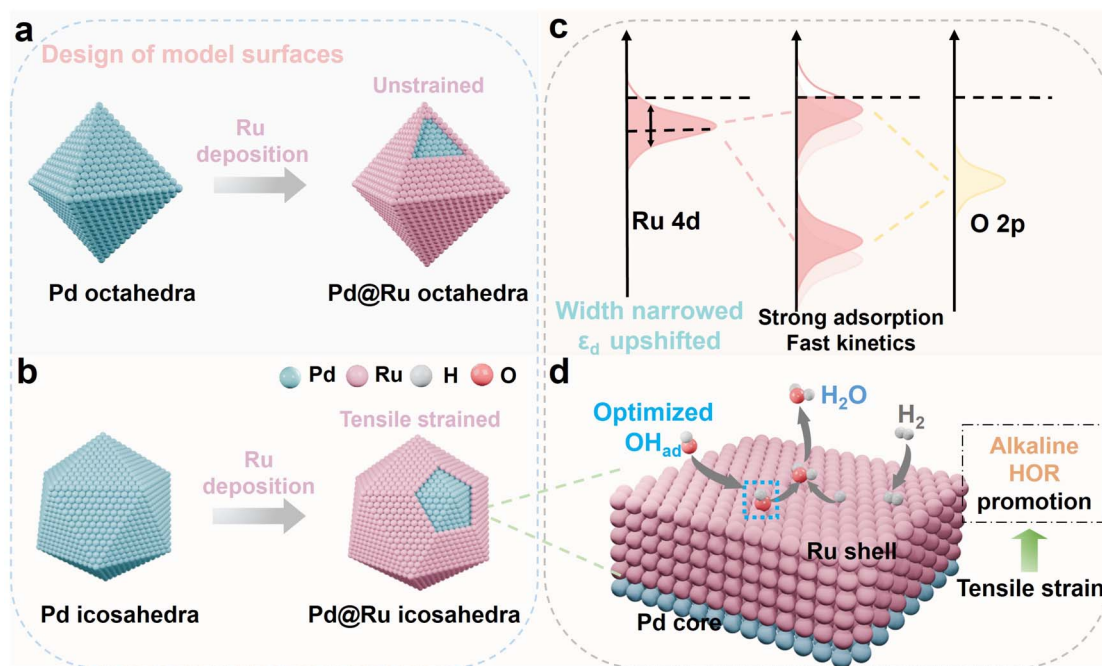
<sup>c</sup>National Laboratory of Solid State Microstructures, School of Electronic Science and Engineering, Collaborative Innovation Center of Advanced Microstructures, Nanjing University, Jiangsu 210023, P. R. China. E-mail: zehuahu@nju.edu.cn

<sup>d</sup>School of Materials Science and Engineering, State Key Laboratory of Silicon and Advanced Semiconductor Materials, Zhejiang University, Hangzhou, Zhejiang 310027, P. R. China

† Electronic supplementary information (ESI) available. See DOI: <https://doi.org/10.1039/d5sc02886h>

‡ These authors contributed equally to this work.





**Scheme 1** Schematic illustration showing the rational design of model surfaces and the strain effect in the alkaline hydrogen oxidation reaction mechanism. (a and b) Scheme of the model surfaces for elucidating the strain effect. (c) Bond formation between the Ru surface and adsorbates upon a tensile strained surface. (d) Origins of the enhanced catalytic performance on the strained surface.

still lacking, limiting the full potential of strain engineering as a tool for improving HOR performance.

Based on the above analyses, we thus aim to construct Ru surfaces with varying strains, while avoiding the interference of the electronic effect, as the model surfaces for investigating the stain effect in alkaline HOR (Scheme 1). To achieve this, five atomic layers of Ru were epitaxially grown on the surfaces of Pd icosahedra (denoted as Pd@Ru icosahedra) or Pd octahedra (denoted as Pd@Ru octahedra). Since the ligand effect between the Pd core and Ru shell is limited within three Ru atomic layers, the as-synthesized Ru surfaces can safely exclude the ligand effect between the Pd core and Ru surface. In the case of the Pd@Ru icosahedra, a tensile strain of 2.5% is induced on the Ru atoms due to lattice enlargement, whereas Pd@Ru octahedra exhibit negligible surface strain (Fig. S1†). Remarkably, the Pd@Ru icosahedra demonstrate a high mass activity of  $2.5 \text{ A mg}_{\text{Ru}}^{-1}$  at 50 mV in alkaline HOR, approximately 2.8 times higher than that of the Pd@Ru octahedra. This activity also significantly surpasses that of commercial Pt/C and Ru/C catalysts by factors of 5.1 and 7.6 times, respectively. Combined with density functional theory (DFT) calculations and experimental evidence, we find that the tensile strain can upshift the d-band center and enhance the adsorption of OH\*, rationalizing the boosted alkaline HOR performance of Pd@Ru icosahedra.

## Results and discussion

### Synthesis and characterization of core-shell Pd@Ru catalysts

To prepare the ideal catalyst model, we synthesized Pd@Ru octahedra and Pd@Ru icosahedra with similar sizes using

a seed-mediated growth method. Briefly, the Pd octahedra enclosed by (111) facets were obtained by transforming Pd cubes through an oxidative etching and regrowth process, following previously reported procedures.<sup>38,39</sup> The Pd icosahedra were directly synthesized in a diethylene glycol (DEG) solution. Subsequently, RuCl<sub>3</sub>·3H<sub>2</sub>O was introduced into the Pd octahedra or Pd icosahedra dispersed in ethylene glycol and heated at 200 °C to achieve the uniform epitaxial growth of the Ru shell. The number of Ru layers was controlled by adjusting the ratio of Pd seed and ruthenium precursors. The key to this precisely controlled synthesis relies on the control of Ru deposition and surface diffusion kinetics, which results in the atomic layer-by-layer deposition on Pd.<sup>38,39</sup> The low-magnification transmission electron microscopy (TEM) images show that the octahedral or icosahedral morphology is well-preserved after Ru deposition (Fig. 1a, b, S2 and S3†). The average sizes of the Pd@Ru octahedra and Pd@Ru icosahedra are determined to be 16.89 nm and 17.62 nm, respectively. The increase in size compared to the Pd seed was approximately 2.29 nm and 2.32 nm, corresponding to the overgrowth of Ru. Besides, Ru nanocages were obtained by selectively etching Pd cores, confirming the successful growth of the Ru shell (Fig. S4†). The crystal phase of core–shell Pd@Ru catalysts was determined by analyzing the XRD pattern (Fig. 1c). All the XRD peaks for the catalysts have symmetric shapes and their positions matched well with those of face-centered-cubic (fcc) Pd (PDF #88-1734), while obvious shifts of diffraction peaks towards lower angles were identified for both Pd icosahedra and Pd@Ru icosahedra, indicating their enlarged lattice. The (111) peak at around 47.4° splits into approximately three peaks for the Pd icosahedra and Pd@Ru



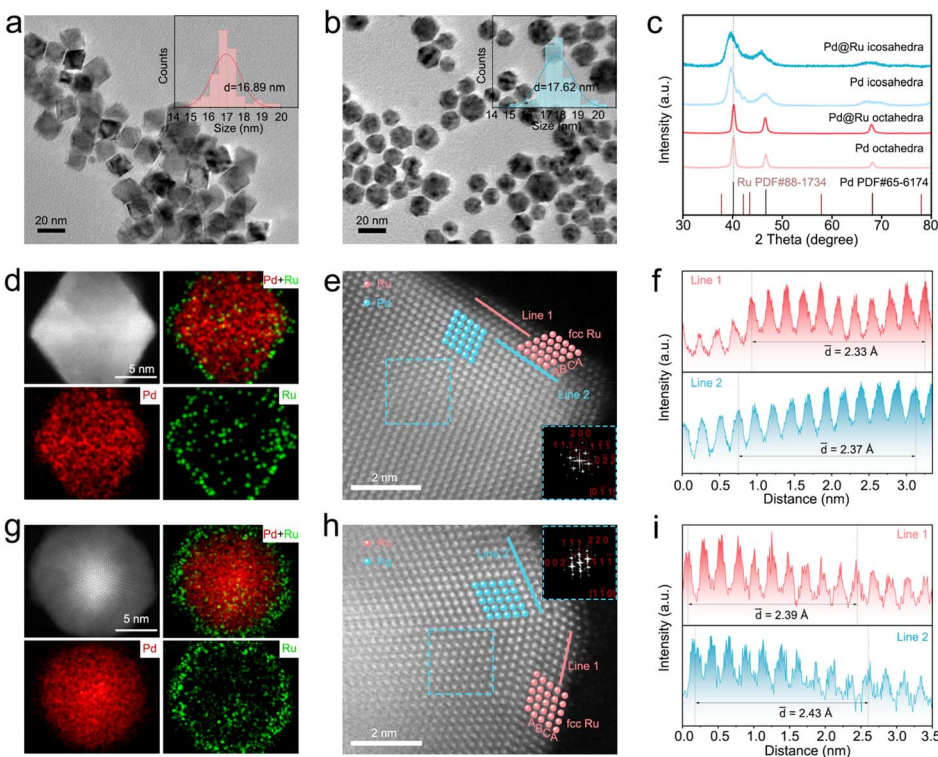


**Fig. 1** Morphology and structure characterization of Pd@Ru octahedral and Pd@Ru icosahedral catalysts. (a and b) Low-magnification TEM images of the Pd@Ru octahedra (a) and Pd@Ru icosahedra (b), and the insets illustrate size distributions. (c) XRD patterns of Pd octahedra, Pd@Ru octahedra, Pd icosahedra and Pd@Ru icosahedra. (d) HAADF-STEM elemental mappings of Pd@Ru octahedra. (e) Atomically resolved HAADF-STEM image of Pd@Ru octahedra. The corresponding FFT pattern was obtained from the region boxed by a blue rectangle. (f) The intensity profiles are obtained along the red and blue lines in (e), respectively. (g) HAADF-STEM elemental mappings of Pd@Ru icosahedra. (h) Atomically resolved HAADF-STEM image of Pd@Ru icosahedra. The corresponding FFT pattern was obtained from the region boxed by a blue rectangle. (i) The intensity profiles are obtained along the red and blue lines in (h), respectively.

icosahedra, arising from the inhomogeneous tensile strain distributed on the Pd icosahedra.<sup>40</sup> In addition, no XRD peaks belonging to Ru were observed, likely due to the similar lattice constants of the Ru shell and the Pd core. The structure and composition of the Pd@Ru catalysts were further characterized using high-angle annular dark-field scanning transmission electron microscopy (HAADF-STEM), energy dispersive X-ray spectroscopy (EDS) and inductively coupled plasma-mass spectrometry (ICP-MS). For the Pd@Ru octahedra, STEM-EDS mapping and the line scan profile (Fig. 1d and S5†) show that Ru atoms are well-distributed on the outer layers of Pd cores, confirming the core–shell structure. The atomic resolution HAADF-STEM image (Fig. 1e) reveals continuous lattice fringes across the interface between the Pd core and the Ru shell, indicating the epitaxial growth of Ru on Pd. According to the ICP-MS data, the Pd/Ru atomic ratio in Pd@Ru octahedra was 1.78, corresponding to approximately five atomic layers (Fig. S5 and Table S1†). The corresponding fast Fourier transform (FFT) pattern from the blue rectangular region in Fig. 1e further confirms the fcc phase structure of Pd octahedra along the [0–11] zone axis. Additionally, the Ru atomic arrangement exhibits a characteristic fcc packing with an ABCABC order, in line with prior studies.<sup>38,41,42</sup> The average measured Ru–Ru distance was 2.333 Å (Fig. 1f and S6†), closely matching the

value of the Ru–Ru distance in bulk Ru crystals (2.33 Å). These findings suggest that the epitaxial growth of five Ru layers on Pd@Ru octahedra shows negligible strain. This result is reasonable considering the slight lattice misfit between Ru and Pd (Pd: 3.89 Å and Ru: 3.82 Å) and the five-atomic-layer configuration of the Ru shell, which enables the relaxation of the lattice misfit. Similarly, the microstructure of the Pd@Ru icosahedra was also confirmed through STEM-EDS mapping and EDS line-scanning profiles (Fig. 1g and S7†). The atomically resolved HAADF-STEM image (Fig. 1h) confirms the successful formation of the Pd@Ru core–shell structure. For an ideal icosahedral model with a core size averaging 15.30 nm and a five-layer Ru shell, the calculated Pd/Ru atomic ratio is 1.89, which closely aligns with the experimentally determined ratio of 1.81 obtained from ICP-MS analysis (Fig. S8 and Table S2†). The corresponding FFT pattern from the blue rectangular region confirms the fcc phase structure of Pd@Ru icosahedra along the [1–10] zone axis (inset in Fig. 1h). The measured average Ru–Ru atomic distance in the Ru shell is 2.39 Å (Fig. 1i). Consequently, the tensile strain in the Ru shell was calculated to be 2.5% using the equation  $S_X = (\alpha_X - \alpha_{\text{bulk}})/\alpha_{\text{bulk}}$  (see the ESI†), where  $\alpha_X$  represents the lattice constant of the Ru shell and  $\alpha_{\text{bulk}}$  is the bulk standard value. Hence, both the XRD and HAADF-STEM analyses confirm the presence of surface tensile strain on

Pd@Ru icosahedra, which is negligible on the Pd@Ru octahedra. It is worth noting that the ligand effect would diminish when the number of shell layers exceeds three, while the strain effect has a long-distance impact, as reported in previous studies.<sup>43–45</sup> To further confirm this, the differential charge density of the Pd@Ru slabs was calculated (Fig. S9†). Notably, when the Ru shell consists of three or fewer layers, a significant electron transfer from Pd to Ru occurs, indicating a strong interaction between the two metals. In contrast, when the Ru shell exceeds four layers, no noticeable charge difference is observed. These results collectively demonstrated that the main difference between our Pd@Ru octahedra and Pd@Ru icosahedra with about five atomic layers lies in the strain effect, making them ideal platforms to investigate the strain effect on their catalytic properties.

To analyze the effects of lattice expansion on the surface chemical states, X-ray photoelectron spectroscopy (XPS) was performed. Both Ru 3d and Pd 3d spectra exhibit doublets, which are deconvoluted into two asymmetric peaks.<sup>46,47</sup> Notably, the Pd 3d<sub>5/2</sub> binding energies of the Pd@Ru icosahedra show a negative shift (around 0.16 eV) compared to that of Pd@Ru octahedra (Fig. 2a–d). In contrast, the Ru 3d<sub>5/2</sub> binding energy of Pd@Ru icosahedra shifts toward a positive value (0.24 eV) compared to that of Pd@Ru octahedra. The result can be attributed to the decreased electron density at the Ru shell with the lattice expansion in Pd@Ru icosahedra.<sup>48</sup> Furthermore, the surface valence band spectra reveal an upshift of the d-band center in the Pd@Ru icosahedra, approximately 0.1 eV higher than that in the Pd@Ru octahedra (Fig. 2e). Meanwhile, we also carried out the projected density of states (PDOS) analysis to theoretically determine the d-band center. This analysis was based on models of fcc-Ru(111) with 2.5% strain and fcc-Ru(111) without strain, representing the Pd@Ru icosahedral and Pd@Ru octahedral catalysts, respectively. The result shows that the d-band center of the

strained Ru(111) surface presents an upward shift relative to the unstrained Ru(111) surface (Fig. 2f). The upshifted d-band center may move more anti-bonding states above the Fermi level, potentially decreasing the occupation of these states and facilitating stronger bonding with intermediates.<sup>49</sup> These results collectively demonstrate that the tensile strain on the Pd@Ru icosahedral surface reduces the electron density and upshifts the d-band center, which may lead to stronger interaction with reaction intermediates.

### Electrocatalytic performance for alkaline HOR

We further evaluated the alkaline HOR performance of the as-prepared Pd@Ru icosahedra and Pd@Ru octahedra by using a rotating disk electrode (RDE) in H<sub>2</sub>-saturated 0.1 M KOH electrolyte. Beforehand, we first loaded Pd@Ru icosahedra and Pd@Ru octahedra onto a Vulcan XC-72 carbon support to obtain the carbon-supported catalysts before the measurements (Fig. S10†). In addition, the commercial Pt/C and homemade Ru/C catalysts (Fig. S11 and S12†) were selected as benchmark catalysts. Fig. 3a shows the polarization curves of all catalysts collected at a scan rate of 1 mV s<sup>−1</sup> with a rotation speed of 1600 rpm. The fastest increase in the anodic current density of the Pd@Ru icosahedra indicates the best HOR activity, which significantly outperforms that of Pd@Ru octahedra (Fig. S13†). The extremely small anode current of Pd@Ru icosahedra in an N<sub>2</sub>-saturated 0.1 M KOH electrolyte demonstrates that the HOR activity stems from H<sub>2</sub> oxidation, rather than from electric double-layer charging (Fig. S14†). Besides, a sharp decline of anode current density after 0.2 V (vs. RHE) can be observed for the Ru/C catalyst, while this phenomenon did not occur on Pd@Ru icosahedra. Then the polarization curves at various speeds ranging from 400 rpm to 2500 rpm were recorded (Fig. 3b). As the rotation speed increases, the anode current density increased due to the improved mass transportation.

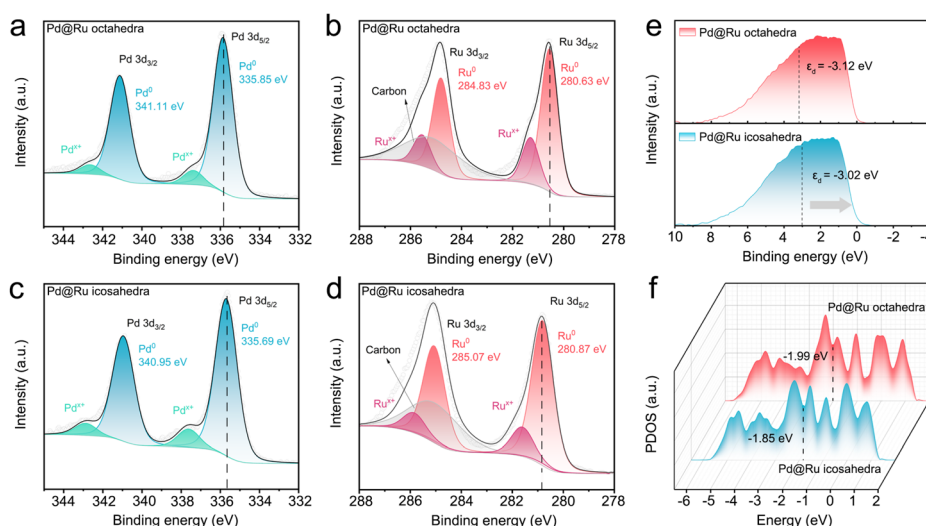


**Fig. 2** Characterization of electronic structures. High-resolution XPS spectra of Pd 3d (a) and Ru 3d (b) in Pd@Ru octahedra. High-resolution XPS spectra of Pd 3d (c) and Ru 3d (d) in Pd@Ru icosahedra. (e) Valence band spectra of Pd@Ru octahedra and Pd@Ru icosahedra as measured by high-resolution XPS. (f) Calculated projected density of states (PDOS) of Ru surfaces for Pd@Ru octahedral and Pd@Ru icosahedral models. The vertical grey lines denote the position of d-band centers.



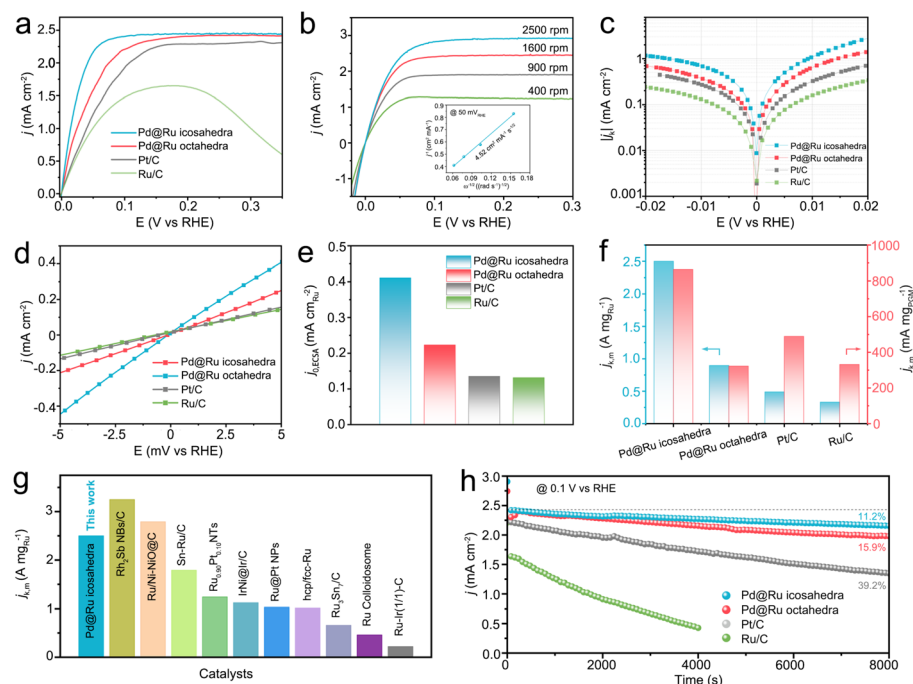


**Fig. 3** Electrocatalytic alkaline hydrogen oxidation reaction (HOR) performance. (a) Polarization curves of Pd@Ru octahedra, Pd@Ru icosahedra, and commercial Pt/C and Ru/C catalysts in  $\text{H}_2$ -saturated 0.1 M KOH solution. Scan rate,  $1 \text{ mV s}^{-1}$ . Rotation speed, 1600 rpm. (b) HOR polarization curves of Pd@Ru icosahedra at different rotation speeds with a scan rate of  $1 \text{ mV s}^{-1}$ . Inset shows the Koutecky–Levich plot at 50 mV (vs. RHE). (c) The HOR/HER Tafel plots of kinetic current density ( $j_k$ ). (d) Linear fitting curves at the micro-polarization region of the HOR/HER. Comparison of specific activity ( $j_0, \text{ECSA}$ ) (e) and mass activity ( $j_{k,m}$ ) (f) at 50 mV. (g) Comparison of the  $j_{k,m}$  of Pd@Ru icosahedra in this work with those of representative alkaline HOR catalysts. (h) Stability tests at 0.1 V (vs. RHE) for different catalysts.

According to the Koutecky–Levich equation, a linear relationship between  $\omega^{-1/2}$  and the inverse of current density ( $j^{-1}$ ) at an overpotential of 50 mV is fitted, obtaining a slope of  $4.52 \text{ cm}^2 \text{ mA}^{-1} \text{ s}^{-1/2}$ . This suggests a two-electron reaction for the HOR process, in accordance with the theoretical value of  $4.87 \text{ cm}^2 \text{ mA}^{-1} \text{ s}^{-1/2}$ .<sup>50</sup>

Next, we examined the Tafel plots from the kinetic current densities ( $j_k$ ) as a function of the potential calculated according to the Koutecky–Levich equation (Fig. 3c), indicating the highest activity of Pd@Ru icosahedra. The exchange current density ( $j_0$ ) of all catalysts was further calculated by the linear fitting of micro-polarization regions (Fig. 3d) and Butler–Volmer fitting. The Pd@Ru icosahedra possess a high geometric  $j_0$  of  $2.24 \text{ mA cm}^{-2}$ , which is the highest compared with that of Pd@Ru octahedra/C ( $1.26 \text{ mA cm}^{-2}$ ), Pt/C ( $0.80 \text{ mA cm}^{-2}$ ), and Ru/C ( $0.70 \text{ mA cm}^{-2}$ ) (Table S3†). To conduct a quantitative comparison of the intrinsic HOR activity of these catalysts, the specific activity ( $j_0, \text{ECSA}$ ) was compared based on the electrochemical active surface area (ECSA)-normalized  $j_0$  (Fig. S15†). As illustrated in Fig. 3e and Table S4,† the HOR-specific activity of Pd@Ru icosahedra ( $0.41 \text{ mA cm}^{-2}$  at 50 mV) is determined to be the best among all catalysts. In particular, mass activity is a significant technical parameter in potential applications. We also normalized the HOR activity to the Ru or PGM loadings on the RDE electrode, and compared the mass activity ( $j_{k,m}$ ). Impressively, as shown in Fig. 3f, the Pd@Ru icosahedra exhibit an unprecedented mass activity of  $2.52 \text{ A mg}_{\text{Ru}}^{-1}$  at an overpotential of 50 mV,

significantly higher than those of Pd@Ru octahedra ( $0.90 \text{ A mg}_{\text{Ru}}^{-1}$ ), the Pt/C catalyst ( $0.49 \text{ A mg}_{\text{Ru}}^{-1}$ ), and the Ru/C catalyst ( $0.33 \text{ A mg}_{\text{Ru}}^{-1}$ ). Besides, the Pd@Ru icosahedra achieve the highest mass activity of  $865 \text{ mA mg}_{\text{PGM}}^{-1}$ . This high performance surpasses that of the most advanced catalysts reported recently (Fig. 3g and Table S5†). In addition, we noted that both  $j_0, \text{ECSA}$  and  $j_{k,m}$  of Pd@Ru icosahedra are higher than that of Pd@Ru octahedra, indicating that the tensile strain on Pd@Ru icosahedra has a pivotal role in improving the HOR kinetics.

The catalytic stability is another important indicator to determine its potential application. The durability of each catalyst was evaluated by applying the potentiostatic method at 0.1 V vs. RHE in  $\text{H}_2$ -saturated 0.1 M KOH at room temperature. Fig. 3h shows that the Pd@Ru icosahedra exhibit negligible decay in the current density (<11.2%) after a continuous 8000 s operation, suggesting their remarkable stability. In contrast, the HOR activity of Pd@Ru octahedra and Pt/C reduced by 15.9% and 39.2%, respectively, and Ru/C ceased to even function after 4000 s due to oxidation. The morphology of the Pd@Ru icosahedra after the stability test was further investigated by TEM. As depicted in Fig. S16,† Pd@Ru icosahedra maintain their icosahedral morphology and uniform distribution on a carbon support, consistent with their excellent stability.

### Mechanistic understanding

The above results explicitly demonstrate that the tensile strain on the surface of a Pd@Ru icosahedron is the key to its superior

HOR activity. We thus conduct DFT calculations to elucidate the underlying mechanisms by which this tensile strain enhances the catalytic activity. Initially, based on the structural parameters from the above experiments, we constructed models for Pd@Ru icosahedra, Pd@Ru octahedra, and Ru/C and Pt/C catalysts, including fcc-Ru(111) with 2.5% strain, fcc-Ru(111) without strain, and hcp-Ru(101) and fcc-Pt(111) slabs as the models, respectively (Fig. 4a). Previous studies have shown that the binding strengths of  $H^*$  (HBE) and  $OH^*$  (OHBE) are closely correlated with HOR activity.<sup>25,51,52</sup> Therefore, we first calculated the adsorption energies of these intermediates on the different slabs. As can be seen from Fig. S17 and S18,<sup>†</sup> the Pd@Ru icosahedra and Pd@Ru octahedra possess very similar  $\Delta E_{OH^*}$  values, indicating that the HBE is not a suitable descriptor in our system. In parallel with the theoretical calculations, we also performed cyclic voltammetry (CV) scans to assess the HBE on various catalysts. The CV results show that the hydrogen adsorption peaks for Pd@Ru icosahedra and Pd@Ru octahedra remain nearly identical (Fig. S19<sup>†</sup>), implying that the HBE of both catalysts has almost no difference. Similarly, in the *in situ* attenuated total reflection surface-enhanced infrared absorption spectroscopy (ATR-SEIRAS) spectra, both catalysts exhibit comparable Ru-H vibrations in the 2000–2130  $cm^{-1}$  range (Fig. S20<sup>†</sup>).<sup>53,54</sup> These findings indicate that the boosted HOR kinetics is likely affected by other reactive intermediates such as the  $OH^*$  intermediate.<sup>55,56</sup>

As depicted in Fig. 4b and S21,<sup>†</sup> the  $OH^*$  adsorption on Pd@Ru icosahedra, Pd@Ru octahedra and Ru/C catalysts is

stronger than that on Pt/C, which is consistent with the intrinsic oxyphilic nature of Ru, as reported in previous studies.<sup>57,58</sup> Remarkably, the  $\Delta E_{OH^*}$  for Pd@Ru icosahedra was calculated to be  $-0.46$  eV, more negative than the value for Pd@Ru octahedra, evidencing the strengthened  $OH^*$  adsorption. Moreover, experimental CO-stripping tests confirm this trend, with the OHBE order as follows: Pd@Ru icosahedra > Pd@Ru octahedra > Ru/C > Pt/C (Fig. 4c). This trend aligns with the alkaline HOR activity, suggesting that the adsorption of hydroxyl ( $OH^*$ ) on the catalyst surface plays a dominant role in alkaline HOR. *In situ* Raman spectroscopy further confirms the adsorption behavior of the catalysts. As shown in Fig. 4d and S22,<sup>†</sup> a weak Ru-OH\* peak was detected at  $802\text{ cm}^{-1}$  for Pd@Ru octahedra. In contrast, an intensified Ru-OH\* binding peak was found at  $795\text{ cm}^{-1}$  for Pd@Ru icosahedra, indicating enhanced OH\* binding strength on the Pd@Ru icosahedra.<sup>59</sup> Indeed, particularly in alkaline media, previous studies imply that enhanced OHBE will benefit the Volmer step for alkaline HOR kinetics.<sup>56</sup> The strengthened OH\* adsorption is primarily attributed to the tensile strain on the Pd@Ru icosahedral surface. To further explore the relationship between the tensile strain of Pd@Ru icosahedra and its strong OH\* adsorption energy, the d-orbital projected density of states (PDOS) was investigated (Fig. S23<sup>†</sup>). According to the d-band center theory, the position of the d-band center can serve as an indicator of the adsorption behavior of OH\* intermediates.<sup>55,60</sup> The results depicted that the tensile strain on the Pd@Ru icosahedra upshifts the d-band center compared to that of Pd@Ru octahedra, Ru/C, and Pt/C.

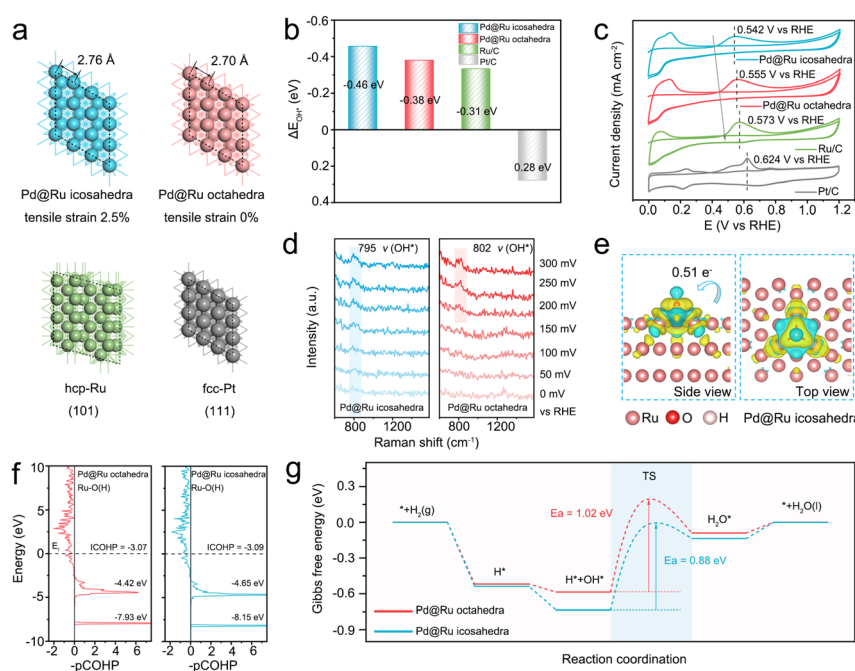


Fig. 4 Mechanistic insights. (a) Optimized structures. (b) The adsorption energy of  $OH^*$  on Pd@Ru octahedra, Pd@Ru icosahedra, and commercial Pt/C and Ru/C catalysts. (c) CO stripping curves for different catalysts. Scan rate,  $20\text{ mV s}^{-1}$ . (d) *In situ* Raman spectra for the HOR occurring on Pd@Ru icosahedral and octahedral surfaces at different potentials in  $H_2$ -saturated  $0.1\text{ M KOH}$  solution. (e) Side and top view of the electronic difference and Bader analysis of Pd@Ru icosahedra. Yellow and blue counters represent the isosurfaces of electronic charge accumulation. (f) The projected crystal orbital Hamilton population ( $-pCOHP$ ) for Ru–O interaction of the  $OH^*$  intermediate on Pd@Ru octahedra (left) and Pd@Ru icosahedra (right). (g) Energetic trend of Pd@Ru octahedra and Pd@Ru icosahedra for the HOR.



Such a trend is consistent with the surface valence band photoemission spectra collected from various catalysts (Fig. S24†). This upward shift reduces the occupied antibonding orbitals and strengthens OH adsorption on the Pd@Ru icosahedral surface. Additional evidence for the stronger OHBE of Pd@Ru icosahedra is obtained through the differential charge density (Fig. 4e and S25†), further highlighting the stronger OH\* adsorption that contributes to the improved HOR kinetics. Moreover, compared to Pd@Ru octahedra, the strained Pd@Ru icosahedra exhibit much stronger orbital hybridization with the O 2p orbital of OH\* (Fig. 4f). These findings not only corroborate the trend in HOR activity for our model catalysts but also provide insights into how tensile strain enhances the catalytic properties of Pd@Ru icosahedra.

Furthermore, the energetic profiles of the HOR pathway for Pd@Ru icosahedra and Pd@Ru octahedra were obtained (Fig. 4g, S26 and S27†). Further analysis of the Volmer step, which involves the combination of reactive OH\* and \*H to produce H<sub>2</sub>O, was conducted to identify the key rate-determining step (Fig. S28†). Corresponding to the DFT results for  $\Delta G_{\text{OH}^*}$ , the reaction barrier for the water generation process was found to be lower on the strained Pd@Ru icosahedra. Specifically, Pd@Ru icosahedra exhibit a significantly lower activation barrier (0.88 eV) compared to Pd@Ru octahedra (1.02 eV). This reduced energy barrier on Pd@Ru icosahedra contributes to its superior HOR activity, aligning with the experimental observations. Taken together, we finally conclude that the tensile strain of Pd@Ru icosahedra plays a pivotal role in enhancing OHBE, thereby improving HOR kinetics in alkaline environments.

## Conclusions

In summary, we have synthesized strained Pd@Ru icosahedra and unstrained Pd@Ru octahedra with similar sizes and surface facets, which serve as well-shaped platforms for efficient alkaline HOR. The strained Pd@Ru icosahedra deliver an impressive mass activity of  $2.5 \text{ A mg}_{\text{Ru}}^{-1}$  at 50 mV, realizing a 2.8-fold enhancement compared to that of the almost unstrained Pd@Ru octahedra toward the HOR. Remarkably, such activity significantly surpasses that of commercial Pt/C and Ru/C catalysts. Furthermore, the Pd@Ru icosahedra present 88.8% retention in current density after 8000 s of the durability test. Mechanistic investigations identify that tensile strain on the Pd@Ru icosahedron surface enhances HOR performance by upshifting the d-band center and strengthening the OH\* adsorption. This accounts for the higher alkaline HOR activity of Pd@Ru icosahedra compared to Pd@Ru octahedra. Overall, this work provides an in-depth understanding of the strain effect in the hydrogen oxidation reaction and implies new opportunities for the design of highly efficient electrocatalysts by strain engineering.

## Data availability

The data that support the findings of this study are available in the ESI† of this article.

## Author contributions

Z. G. and H. H. developed the concept. Z. G. performed the syntheses. Z. G. and Y. Q. conducted the writing and visualization. Z. G., Y. W., M. L., Z. G., Z. H. and Y. L. performed the characterization. Y. L., J. Y. and L. Z. revised the manuscript. Y. Q. and H. H. supervised the project.

## Conflicts of interest

There are no conflicts to declare.

## Acknowledgements

This work was supported by the National Key Research and Development Program of China (No. 2021YFA1502000), NSFC (No. 22322902, U22A20396, and 22211540385), the Science and Technology Innovation Program of Hunan Province (No. 2021RC3065), the Jiebang Guashuai Project of Changsha City (No. kq2301009), the Postgraduate Scientific Research Innovation Project of Hunan Province (No. CX20230455), the Guangdong Basic and Applied Basic Research Foundation (No. 2024A1515012350), and the Shenzhen Science and Technology Program (No. JCYJ20210324120800002, JCYJ20220818100012025, and JCYJ20230807122007015). The authors also thank the Analytical Instrumentation Center of Hunan University for *in situ* Raman measurements (WITec Alpha 300R).

## Notes and references

- 1 I. Dincer, Renewable Energy and Sustainable Development: A Crucial Review, *Renewable Sustainable Energy Rev.*, 2000, **4**, 157–175.
- 2 D. Gielen, F. Boshell, D. Saygin, M. D. Bazilian, N. Wagner and R. Gorini, The Role of Renewable Energy in the Global Energy Transformation, *Energy Strategy Rev.*, 2019, **24**, 38–50.
- 3 S. Gottesfeld, D. R. Dekel, M. Page, C. Bae, Y. Yan, P. Zelenay and Y. S. Kim, Anion Exchange Membrane Fuel Cells: Current Status and Remaining Challenges, *J. Power Sources*, 2018, **375**, 170–184.
- 4 M. Hren, M. Božić, D. Fakin, K. S. Kleinschek and S. Gorgieva, Alkaline Membrane Fuel Cells: Anion Exchange Membranes and Fuels, *Sustainable Energy Fuels*, 2021, **5**, 604–637.
- 5 F. Li, S. H. Chan and Z. Tu, Recent Development of Anion Exchange Membrane Fuel Cells and Performance Optimization Strategies: A Review, *Chem. Rec.*, 2024, **24**, e202300067.
- 6 V. M. Truong, N. B. Duong, C. L. Wang and H. Yang, Effects of Cell Temperature and Reactant Humidification on Anion Exchange Membrane Fuel Cells, *Materials*, 2019, **12**, 2048.
- 7 S. Zhang, R. Ren, J. Cao, D. Zhang, J. Bai, C. Han, L. Xiao, L. Zhuang, P. Song and W. Xu, Ru-MnO Heterostructure Clusters Toward Efficient and CO-Tolerant Alkaline Hydrogen Oxidation Reaction, *Adv. Energy Mater.*, 2024, **15**, 2404266.



8 Y.-P. Ku, K. Ehelebe, A. Hutzler, M. Bierling, T. Böhm, A. Zitolo, M. Vorokhta, N. Bibent, F. D. Speck, D. Seeberger, I. Khalakhan, K. J. J. Mayrhofer, S. Thiele, F. Jaouen and S. Cherevko, Oxygen Reduction Reaction in Alkaline Media Causes Iron Leaching from Fe-N-C Electrocatalysts, *J. Am. Chem. Soc.*, 2022, **144**, 9753–9763.

9 L. Huang, H. Niu, C. Xia, F.-M. Li, Z. Shahid and B. Y. Xia, Integration Construction of Hybrid Electrocatalysts for Oxygen Reduction, *Adv. Mater.*, 2024, **36**, 2404773.

10 H. Chen, R. Tao, K.-T. Bang, M. Shao and Y. Kim, Anion Exchange Membranes for Fuel Cells: State-of-the-Art and Perspectives, *Adv. Energy Mater.*, 2022, **12**, 2200934.

11 P. S. Lamoureux, A. R. Singh and K. Chan, pH Effects on Hydrogen Evolution and Oxidation over Pt(111): Insights from First-Principles, *ACS Catal.*, 2019, **9**, 6194–6201.

12 N. Ramaswamy, S. Ghoshal, M. K. Bates, Q. Jia, J. Li and S. Mukerjee, Hydrogen Oxidation Reaction in Alkaline Media: Relationship between Electrocatalysis and Electrochemical Double-Layer Structure, *Nano Energy*, 2017, **41**, 765–771.

13 S. S. John, R. W. Atkinson, A. Roy, R. R. Unocic, A. B. Papandrew and T. A. Zawodzinski, The Effect of Carbonate and pH on Hydrogen Oxidation and Oxygen Reduction on Pt-Based Electrocatalysts in Alkaline Media, *J. Electrochem. Soc.*, 2016, **163**, F291.

14 J.-T. Ren, L. Chen, H.-Y. Wang, Y. Feng and Z.-Y. Yuan, Hydrogen Oxidation Electrocatalysts for Anion-Exchange Membrane Fuel Cells: Activity Descriptors, Stability Regulation, and Perspectives, *Energy Environ. Sci.*, 2024, **17**, 3960–4009.

15 C. Hu, J. Xu, Y. Tan and X. Huang, Recent Advances of Ruthenium-based Electrocatalysts for Hydrogen Energy, *Trends Chem.*, 2023, **5**, 225–239.

16 A. G. Oshchepkov, G. Braesch, A. Bonnefont, E. R. Savinova and M. Chatenet, Recent Advances in the Understanding of Nickel-Based Catalysts for the Oxidation of Hydrogen-Containing Fuels in Alkaline Media, *ACS Catal.*, 2020, **10**, 7043–7068.

17 D. Tang, J. Pan, S. Lu, L. Zhuang and J. Lu, Alkaline Polymer Electrolyte Fuel Cells: Principle, Challenges, and Recent Progress, *Sci. China: Chem.*, 2010, **53**, 357–364.

18 L. Wei, W. Yan, Z. Huang, R. Li, Q. Kong, W.-H. Huang, C.-W. Pao, Z. Hu, H. Lin, N. Chen, Y. Xu, H. Geng and X. Huang, Phase and Interface Engineering of a Ru-Sn Nanocatalyst for Enhanced Alkaline Hydrogen Oxidation Reaction, *Energy Environ. Sci.*, 2024, **17**, 5922–5930.

19 J. Zhang, M. Cao, X. Li, Y. Xu, W. Zhao, L. Chen, Y.-C. Chang, C.-W. Pao, Z. Hu and X. Huang, Kinetic-Modulated Crystal Phase of Ru for Hydrogen Oxidation, *Small*, 2023, **19**, 2207038.

20 Y. Li, C. Yang, J. Yue, H. Cong and W. Luo, Polymorphism-Interface-Induced Work Function Regulating on Ru Nanocatalyst for Enhanced Alkaline Hydrogen Oxidation Reaction, *Adv. Funct. Mater.*, 2023, **33**, 2211586.

21 Q. Yao, S.-Y. Lv, Z. Yu, Y.-C. Chang, C.-W. Pao, Z. Hu, L.-M. Yang, X. Huang, Q. Shao and J. Lu, Face-Centered Cubic Ruthenium Nanocrystals with Promising Thermal Stability and Electrocatalytic Performance, *ACS Catal.*, 2023, **13**, 11023–11032.

22 Z. Yang, W. Lai, B. He, J. Wang, F. Yu, Q. Liu, M. Liu, S. Zhang, W. Ding, Z. Lin and H. Huang, Tailoring Interfacial Chemistry of Defective Carbon-Supported Ru Catalyst Toward Efficient and CO-Tolerant Alkaline Hydrogen Oxidation Reaction, *Adv. Energy Mater.*, 2023, **13**, 2300881.

23 Z. Liang, H. Liu, S. Huang, M. Xing, Z. Li, S. Wang, L. Yang and D. Cao, Ruthenium Nanoparticles Supported on Ni<sub>3</sub>N Nanosheets as Bifunctional Electrocatalysts for Hydrogen Oxidation/Evolution Reactions, *J. Mater. Chem. A*, 2023, **11**, 849–857.

24 C. A. Campos-Roldán, R. Chattot, F. Pailloux, A. Zitolo, J. Rozière, D. J. Jones and S. Cavaliere, Lanthanide Contraction Effect on the Alkaline Hydrogen Evolution and Oxidation Reactions Activity in Platinum-Rare Earth Nanoalloys, *J. Mater. Chem. A*, 2024, **12**, 1253–1258.

25 C. Zhan, Y. Xu, L. Bu, H. Zhu, Y. Feng, T. Yang, Y. Zhang, Z. Yang, B. Huang, Q. Shao and X. Huang, Subnanometer High-Entropy Alloy Nanowires Enable Remarkable Hydrogen Oxidation Catalysis, *Nat. Commun.*, 2021, **12**, 6261.

26 M. K. Kabiraz, B. Ruqia, J. Kim, H. Kim, H. J. Kim, Y. Hong, M. J. Kim, Y. K. Kim, C. Kim, W.-J. Lee, W. Lee, G. H. Hwang, H. C. Ri, H. Baik, H.-S. Oh, Y. W. Lee, L. Gao, H. Huang, S. M. Paek, Y.-J. Jo, C. H. Choi, S. W. Han and S.-I. Choi, Understanding the Grain Boundary Behavior of Bimetallic Platinum-Cobalt Alloy Nanowires toward Oxygen Electro-Reduction, *ACS Catal.*, 2022, **12**, 3516–3523.

27 M. Feng, J. Huang, Y. Peng, C. Huang, X. Yue and S. Huang, Tuning the Electronic Structures of Cobalt-Molybdenum Bimetallic Carbides to boost the Hydrogen Oxidation Reaction in Alkaline Medium, *Chem. Eng. J.*, 2022, **428**, 131206.

28 L. Wang, Z. Xu, C.-H. Kuo, J. Peng, F. Hu, L. Li, H.-Y. Chen, J. Wang and S. Peng, Stabilizing Low-Valence Single Atoms by Constructing Metalloid Tungsten Carbide Supports for Efficient Hydrogen Oxidation and Evolution, *Angew. Chem., Int. Ed.*, 2023, **62**, e202311937.

29 W. Ni, J. L. Meibom, N. U. Hassan, M. Chang, Y.-C. Chu, A. Krammer, S. Sun, Y. Zheng, L. Bai, W. Ma, S. Lee, S. Jin, J. S. Luterbacher, A. Schüller, H. M. Chen, W. E. Mustain and X. Hu, Synergistic Interactions between PtRu Catalyst and Nitrogen-Doped Carbon Support boost Hydrogen Oxidation, *Nat. Catal.*, 2023, **6**, 773–783.

30 T. He, W. Wang, F. Shi, X. Yang, X. Li, J. Wu, Y. Yin and M. Jin, Mastering the Surface Strain of Platinum Catalysts for Efficient Electrocatalysis, *Nature*, 2021, **598**, 76–81.

31 M. Mavrikakis, B. Hammer and J. K. Nørskov, Effect of Strain on the Reactivity of Metal Surfaces, *Phys. Rev. Lett.*, 1998, **81**, 2819–2822.

32 M. Li, Z. Zhao, Z. Xia, M. Luo, Q. Zhang, Y. Qin, L. Tao, K. Yin, Y. Chao, L. Gu, W. Yang, Y. Yu, G. Lu and S. Guo, Exclusive Strain Effect Boosts Overall Water Splitting in PdCu/Ir Core/Shell Nanocrystals, *Angew. Chem., Int. Ed.*, 2021, **60**, 8243–8250.



33 Q. Wu, W. Yang, X. Wang, W. Zhu, S. Lv, Y. Zhou, T. Chen, S. Liu, W. Li and Z. Chen, Inherent Vacancy of Compressive Ru Nanoparticles Accelerate Electro-Catalytic Hydrogen Energy Conversion, *Appl. Catal., B*, 2023, **335**, 122896.

34 M. Wang, C. Tang, S. Geng, C. Zhan, L. Wang, W.-H. Huang, C.-W. Pao, Z. Hu, Y. Li, X. Huang and L. Bu, Compressive Strain in Platinum-Iridium-Nickel Zigzag-Like Nanowire Boosts Hydrogen Catalysis, *Small*, 2024, **20**, 2310036.

35 X. Wang, S.-I. Choi, L. T. Roling, M. Luo, C. Ma, L. Zhang, M. Chi, J. Liu, Z. Xie, J. A. Herron, M. Mavrikakis and Y. Xia, Palladium-Platinum Core-Shell Icosahedra with Substantially Enhanced Activity and Durability towards Oxygen Reduction, *Nat. Commun.*, 2015, **6**, 7594.

36 J. Kim, H. Kim, W.-J. Lee, B. Ruqia, H. Baik, H.-S. Oh, S.-M. Paek, H.-K. Lim, C. H. Choi and S.-I. Choi, Theoretical and Experimental Understanding of Hydrogen Evolution Reaction Kinetics in Alkaline Electrolytes with Pt-Based Core-Shell Nanocrystals, *J. Am. Chem. Soc.*, 2019, **141**, 18256–18263.

37 S. Zhu, X. Qin, F. Xiao, S. Yang, Y. Xu, Z. Tan, J. Li, J. Yan, Q. Chen, M. Chen and M. Shao, The Role of Ruthenium in Improving the Kinetics of Hydrogen Oxidation and Evolution Reactions of Platinum, *Nat. Catal.*, 2021, **4**, 711–718.

38 M. Zhao, A. O. Elnabawy, M. Vara, L. Xu, Z. D. Hood, X. Yang, K. D. Gilroy, L. Figueroa-Cosme, M. Chi, M. Mavrikakis and Y. Xia, Facile Synthesis of Ru-Based Octahedral Nanocages with Ultrathin Walls in a Face-Centered Cubic Structure, *Chem. Mater.*, 2017, **29**, 9227–9237.

39 J. Zhao, M. Wang, Y. Peng, J. Ni, S. Hu, J. Zeng and Q. Chen, Exploring the Strain Effect in Single Particle Electrochemistry using Pd Nanocrystals, *Angew. Chem., Int. Ed.*, 2023, **62**, e202304424.

40 H. Huang, H. Jia, Z. Liu, P. Gao, J. Zhao, Z. Luo, J. Yang and J. Zeng, Understanding of Strain Effects in the Electrochemical Reduction of CO<sub>2</sub> : Using Pd Nanostructures as an Ideal Platform, *Angew. Chem., Int. Ed.*, 2017, **56**, 3594–3598.

41 M. Zhao, L. Xu, M. Vara, A. O. Elnabawy, K. D. Gilroy, Z. D. Hood, S. Zhou, L. Figueroa-Cosme, M. Chi, M. Mavrikakis and Y. Xia, Synthesis of Ru Icosahedral Nanocages with a Face-Centered-Cubic Structure and Evaluation of Their Catalytic Properties, *ACS Catal.*, 2018, **8**, 6948–6960.

42 M. Zhao, L. Figueroa-Cosme, A. O. Elnabawy, M. Vara, X. Yang, L. T. Roling, M. Chi, M. Mavrikakis and Y. Xia, Synthesis and Characterization of Ru Cubic Nanocages with a Face-Centered Cubic Structure by Templatting with Pd Nanocubes, *Nano Lett.*, 2016, **16**, 5310–5317.

43 S. Bai, C. Wang, M. Deng, M. Gong, Y. Bai, J. Jiang and Y. Xiong, Surface Polarization Matters: Enhancing the Hydrogen-Evolution Reaction by Shrinking Pt Shells in Pt-Graphene Stack Structures, *Angew. Chem., Int. Ed.*, 2014, **53**, 12120–12124.

44 Y. Guo, B. Hou, X. Cui, X. Liu, X. Tong and N. Yang, Pt Atomic Layers Boosted Hydrogen Evolution Reaction in Nonacidic Media, *Adv. Energy Mater.*, 2022, **12**, 2201548.

45 M. Klimenkov, S. Nepijko, H. Kuhlenbeck, M. Bäumer, R. Schlögl and H. J. Freund, The Structure of Pt-Aggregates on a Supported Thin Aluminum Oxide Film in Comparison with Unsupported Alumina: a Transmission Electron Microscopy Study, *Surf. Sci.*, 1997, **391**, 27–36.

46 J. Z. Y. Seow and T. D. Nguyen, Electrochemically Assisted Synthesis of Ultra-Small Ru@IrO<sub>x</sub> Core-Shell Nanoparticles for Water Splitting Electrocatalysis, *Electrochim. Acta*, 2020, **341**, 136058.

47 T. Wang, L.-Y. Li, L.-N. Chen, T. Sheng, L. Chen, Y.-C. Wang, P. Zhang, Y.-H. Hong, J. Ye, W.-F. Lin, Q. Zhang, P. Zhang, G. Fu, N. Tian, S.-G. Sun and Z.-Y. Zhou, High CO-Tolerant Ru-Based Catalysts by Constructing an Oxide Blocking Layer, *J. Am. Chem. Soc.*, 2022, **144**, 9292–9301.

48 H. Guo, L. Li, Y. Chen, W. Zhang, C. Shang, X. Cao, M. Li, Q. Zhang, H. Tan, Y. Nie, L. Gu and S. Guo, Precise Strain Tuning Boosts Electrocatalytic Hydrogen Generation, *Adv. Mater.*, 2023, **35**, 2302285.

49 Q. Hu, K. Gao, X. Wang, H. Zheng, J. Cao, L. Mi, Q. Huo, H. Yang, J. Liu and C. He, Subnanometric Ru clusters with Upshifted D band Center Improve Performance for Alkaline Hydrogen Evolution Reaction, *Nat. Commun.*, 2022, **13**, 3958.

50 Z. Zhuang, S. A. Giles, J. Zheng, G. R. Jenness, S. Caratzoulas, D. G. Vlachos and Y. Yan, Nickel Supported on Nitrogen-Doped Carbon Nanotubes as Hydrogen Oxidation Reaction Catalyst in Alkaline Electrolyte, *Nat. Commun.*, 2016, **7**, 10141.

51 Y.-H. Wang, X.-T. Wang, H. Ze, X.-G. Zhang, P. M. Radjenovic, Y.-J. Zhang, J.-C. Dong, Z.-Q. Tian and J.-F. Li, Spectroscopic Verification of Adsorbed Hydroxy Intermediates in the Bifunctional Mechanism of the Hydrogen Oxidation Reaction, *Angew. Chem., Int. Ed.*, 2021, **60**, 5708–5711.

52 D. Strmenik, M. Uchimura, C. Wang, R. Subbaraman, N. Danilovic, D. van der Vliet, A. P. Paulikas, V. R. Stamenkovic and N. M. Markovic, Improving the Hydrogen Oxidation Reaction Rate by Promotion of Hydroxyl Adsorption, *Nat. Chem.*, 2013, **5**, 300–306.

53 L. Wei, Y. Dong, W. Yan, Y. Zhang, C. Zhan, W.-H. Huang, C.-W. Pao, Z. Hu, H. Lin, Y. Xu, H. Geng and X. Huang, Hollow Pt-Encrusted RuCu Nanocages Optimizing OH Adsorption for Efficient Hydrogen Oxidation Electrocatalysis, *Angew. Chem., Int. Ed.*, 2025, **64**, e202420177.

54 Y. Xue, L. Shi, X. Liu, J. Fang, X. Wang, B. P. Setzler, W. Zhu, Y. Yan and Z. Zhuang, A Highly-Active, Stable and Low-Cost Platinum-Free Anode Catalyst Based on RuNi for Hydroxide Exchange Membrane Fuel Cells, *Nat. Commun.*, 2020, **11**, 5651.

55 L. Su, Y. Jin, D. Gong, X. Ge, W. Zhang, X. Fan and W. Luo, The Role of Discrepant Reactive Intermediates on Ru-Ru<sub>2</sub>P Heterostructure for pH-Universal Hydrogen Oxidation Reaction, *Angew. Chem., Int. Ed.*, 2023, **62**, e202215585.



56 J. Yue, Y. Li, C. Yang and W. Luo, Hydroxyl-Binding Induced Hydrogen Bond Network Connectivity on Ru-based Catalysts for Efficient Alkaline Hydrogen Oxidation Electrocatalysis, *Angew. Chem., Int. Ed.*, 2025, **64**, e202415447.

57 Q. He, Y. Zhou, H. Shou, X. Wang, P. Zhang, W. Xu, S. Qiao, C. Wu, H. Liu, D. Liu, S. Chen, R. Long, Z. Qi, X. Wu and L. Song, Synergic Reaction Kinetics over Adjacent Ruthenium Sites for Superb Hydrogen Generation in Alkaline Media, *Adv. Mater.*, 2022, **34**, 2110604.

58 X. Zhang, L. Xia, G. Zhao, B. Zhang, Y. Chen, J. Chen, M. Gao, Y. Jiang, Y. Liu, H. Pan and W. Sun, Fast and Durable Alkaline Hydrogen Oxidation Reaction at the Electron-Deficient Ruthenium-Ruthenium Oxide Interface, *Adv. Mater.*, 2023, **35**, 2208821.

59 F. Lin, H. Luo, L. Li, F. Lv, Y. Chen, Q. Zhang, X. Han, D. Wang, M. Li, Y. Luo, K. Wang, L. Gu, Q. Wang, X. Zhao, M. Luo and S. Guo, Synthesis of Isolated Ru-O<sub>3</sub> Sites on Hexagonal Close-Packed Intermetallic Penta-Metallene for Hydrogen Oxidation Electrocatalysis, *Nat. Synth.*, 2025, **4**, 399–409.

60 B. Hammer and J. K. Nørskov, Electronic Factors Determining the Reactivity of Metal Surfaces, *Surf. Sci.*, 1995, **343**, 211–220.

